http://www.aimspress.com/journal/energy

AIMS Energy, 9(4): 727–754.
DOI: 10.3934/energy.2021034
Received: 09 February 2021
Accepted: 08 June 2021
Published: 16 June 2021

Research article

Model for measuring concentration ratio distribution of a dish concentrator using moonlight as a precursor for solar tower flux mapping

Minghuan Guo[1,2,*], Hao Wang[1,2], Zhifeng Wang[1,2], Xiliang Zhang[1,3], Feihu Sun[1,3] and Nan Wang[4]

[1] Institute of Electrical Engineering, Chinese Academy of Sciences, No.6 Beiertiao, Zhongguancun, Haidian District, Beijing, 100190, China
[2] School of Engineering Science, University of Chinese Academy of Sciences, No. 380, Huaibei Town, Huairou District, Beijing, 101408, China
[3] Beijing Engineering Research Center of Solar Thermal Power, No.6 Beiertiao, Zhongguancun, Haidian District, Beijing, 100190, China
[4] State Grid Shanxi Electric Power Research Institute, No. 6, Qingnian Road, Yingze District, Taiyuan City, Shanxi Province, 030000, China

* **Correspondence:** Email: guominghuan@mail.iee.ac.cn; Tel: +861082547139.

Abstract: Measuring solar flux distribution (also called flux mapping) of a large receiver is quite challenging. Lunar flux mapping measures the illuminance distribution on the receiver aperture and the direct normal lunar illuminance during moonlight concentration experiments to determine the concentration ratio distribution (CRD). This paper presents a new lunar flux mapping model to extend the applicability to parts of the lunar cycle where the moon is not full. A dish concentrator with a similar concentration ratio to a tower concentrator was built in Beijing and used for lunar flux mapping experiments. A general method of backward ray tracing with effective sun/moon shapes for simulation of CRD is developed. The moonshape image and the normalized error image are convolved in two dimensions using the Fast Fourier Transform to give the effective moon shape image. Several optical simulations and moonlight concentration measurements on the concentrator show good similarity in the effects of changes in light source shape between solar and lunar CRD images. This model recognizes the potential of a solar concentrator to enhance the similarity between the solar CRD and a lunar CRD and that the residual differences can be compensated to some extent by using the smoothing filtering of the lunar CRD image to approximate the expected solar CRD image. The cosine similarity between lunar and solar CRDs is a function of the cosine similarity between the corresponding light source shapes, which can be derived from the dish concentrator and shows promise for application to a large solar tower system.

Keywords: solar tower concentrator; moonlight concentration; flux mapping; solar dish; concentration ratio distribution; smoothing filter; cosine similarity

1. Introduction

A large number of heliostats in the solar field of a solar thermal tower power plant concentrate sunlight onto the receiver on the tower, together forming a high-intensity, high-temperature, non-uniform energy flux distribution on the aperture of the receiver. The energy flux density distribution changes continually with time. The aperture is the natural interface of energy flow between the solar field and the receiver. For experimental evaluation of the optical efficiency of the solar field and the thermal efficiency of the receiver, optimization of the aiming strategy of each heliostat, control of flux distribution on the receiver surface, and the dynamic adjustment of the operation strategy of the receiver, it is necessary to measure the concentrated solar flux density distribution on the receiver aperture. However, measuring the flux on a large receiver in a practical solar tower power plant is challenging, because of the extreme conditions mentioned above. Ballestrín et al. gave a good summary of heat flux measurement technologies for concentrating solar power as a book chapter [1].

Many measuring methods of the concentrated solar flux density distribution have been reported in recent decades. Generally, the measuring methods can be divided into three categories: direct, indirect, and other methods. Direct measurement refers to the use of an array of heat flux sensors. This has high measurement accuracy but low spatial resolution. Indirect measurement refers to the use of a camera and a diffuse reflection target. The spatial resolution of the indirect measurement is high, but the accuracy of the energy flux value is low.

Water-cooled heat flux gauges were installed in an array on the inside wall of the cavity receiver of the PS-10 solar tower power plant, and the concentrated solar flux density distribution was directly measured [2]. There are good pratical examples of the direct measurement method for solar flux mapping on small central receivers with stationary or scanning heat flux sensors [3–6]. The spatial resolution of the measured solar flux distribution was then enhanced by interpolation. Using a moving array of sensors in the direct measuring method increases the mechanical complexity of the system. The typical indirect measurement method is the camera-target method, which usually uses a moving white board to diffusely reflect the concentrated solar beam, a CCD camera in the heliostat field to capture the concentrated solar images, and one or two reference heat flux sensors to calibrate the measurements from gray image to flux image [7–10]. Röger et al. [11] summarized the existing direct and indirect moving bar techniques. They presented a new measurement-supported optical simulation technique, which depended on accurate evaluation of the reflectivity distribution over the receiver surface, and mirror surface measurements for ray tracing. Ho et al. [12–14] developed the flux mapping method of PHLUX (Photographic Flux mapping) for external central receivers. It only took images of the sun and the concentrated solar image on the receiver surface using the same camera settings. The pixel grey values of the shot images were calibrated to the flux density using the direct normal solar irradiance (DNI), and the solar flux distribution was obtained. Xiao et al. [15] repeated the flux mapping method of PHLUX and conducted experiments on a mirror facet on a rooftop. PHLUX still needs accurate reflectivity distribution of the receiver surface. As experiments show, when the heliostat field concentrates the sun lights onto the receiver aperture with one aiming point only, the concentrated solar flux density distribution is always close to an elliptical-Gaussian distribution. So the authors [16] have proposed a radical imaging (mapping) method of solar flux density over the large receiver aperture from the measured flux density values from the sensors on the aperture boundaries using the boundary interpolation reconstruction technique. When the heliostats in the field track the sun with multiple aim points on the receiver aperture, or the concentrated solar flux density distribution much a bit deviates from an elliptical-Gaussian distribution, the flux density distribution should be estimated by optical modeling and best fitted with a mixture of several bivariate functions which are suitable for interpolation reconstruction. Thus, the flux density distribution for each component function can be reconstructed separately. The sum of the reconstructed flux density distributions gives the total flux density distribution on the receiver aperture. But in practice, it is too hard, and more information is needed due to the limited boundary measurements with relatively large measurement errors and the irregular patterns of flux density distribution. For the initial evaluation of the concentration of the entire heliostat field, some moonlight concentration tests of the heliostat field can be carried out on some clear nights, following the working modes in the daytime. Then some typical concentrated solar flux density distributions are directly measured, combining with DNI data.

Moonlight experiments on solar facilities are not new. There were some related studies on optical performances of point-focusing solar collectors in clear full moon nights in the past few decades. Since the moon subtends approximately the same angle as the sun, the camera-target flux mapping using the full moon as the light source, rather than the sun, was often used to evaluate the optical quality of solar concentrators. Hisada et al. [17] at Nagoya Municipal Industrial Research Institute (NMIRI) studied the moonlight concentration of the solar furnace in a full moon night to figure out the optical accuracy of the mirror surface. The moonlight concentration was carried out on May 7th of 1980; 205 heliostats of the Central Receiver Test Facility of SNL were orderly operated to concentrate moonlight onto the white target of the BCS for mirror facet canting of the heliostats [18]. Moonlight experiments were also performed at the THEMIS solar power plant to evaluate the optical defects of the mirrors and not predict solar flux mapping [19]. Full moon flux mapping was used to characterize the ANU 400 m^2 "Big Dish" solar concentrator [20]. Lunar flux mapping was also utilized on the PETAL 400 m^2 dish at Ben-Gurion University, Sede Boqer Campus, Israel [21]. They found good agreement between the compound flux distribution calculated from the individual panel measurements and the expected solar flux distribution calculated from the moon flux maps. On Sept. 4th of 2009, the full moon flux mapping was applied on the 500 m^2 "Big Dish" to evaluate the optical errors at the Australian National University, Canberra, Australia [22]. For investigating the optical error parameters, Blázquez et al. [23] carried out the moonlight concentration tests on the DS1 solar dish of the SOLARDIS project in Spain on July 23rd of 2014. Experimental flux distributions were measured during a full moon night with 30 heliostats on THEMIS solar tower to validate the optical simulation model and the optimized aiming point strategy [24]. Moonlight concentration experiments were carried out at the Badaling Solar Tower Power Plant in Beijing on the full moon night of Sept. 24th, 2018 [25,26]. That method measured illuminance distribution on the receiver aperture using a stationary array of illuminometers and the direct normal lunar illuminance (DNImoon) using a reference illuminometer on the dual-axis moon tracker. The concentrated solar flux density F(x, y) could be obtained by

$$F(x,y) = CR(x,y)sun \cdot DNIsun = CR(x,y)moon \cdot DNIsun,$$

using the assumption that the lunar concentration ratio distribution be equal to the solar concentration ratio distribution, i.e.,

$$CR(x,y)sun = CR(x,y)moon = I(x,y)/DNImoon,$$

where I(x,y) is the illuminance distribution.

In reality, the ideal case of CR(x,y)sun = CR(x,y)moon should not hold. The non radial symetrysse and the difference between the spetra of sunlight and moonlight limit attempts to correlate the lunar illuminance to the solar flux at any given point in the flux distribution. Moreover, the periodical chang of moon shape with the phase of the moon and the very few clear full moon nights limit the broad application of lunar flux mapping to a central receiver system for indirect solar flux measurements.

The above solar flux mapping and full-moon light concentration activities are summarized in Table 1. The moonlight concentration experiments were all conducted on point-focusing solar concentrators (solar dish concentrator, solar furnace, or central receiver system), either for the purpose of indirect flux measurement or for investigating the optical errors of mirrors. Although moonlight concentration activities have a long history, the indirect methods of moonlight flux mapping for a heliostat field are still immature due to the few days available in a month when the phase of the moon is greater than 95%.

Table 1. Flux mapping research and moonlight concentration experiments on point-focusing solar concentrators.

Flux measurement activities	Published year	Research unit	Motivation	Light source
Summary of heat flux measurement and flux mapping systems [1]	2012	CIEMAT-PSA, Spain; ANU, Australia	Summary	Sun/noon
Heat flux gauges used on the receiver of PS10 solar tower plant [2]	2006	Abengoa, Spain	Direct flux measurement	sun
MDF system (moving bar with eight calorimeters) on the receiver of SSPS-CRS tower [3]	2002	CIEMAT-PSA, Spain	Direct flux measurement	sun
Hybrid heat flux measurement system on the receiver of SSPS-CRS tower [4]	2004	CIEMAT-PSA, Spain	"Direct + indirect" flux measurement	sun
Improved MDF (moving bar with eight radiometers) on the receiver of SSPS-CRS tower [5]	2010	CIEMAT-PSA, Spain	Direct flux measurement	sun
Hybrid flux measurement on receiver of SSPS-CRS tower [6]	2013	CIEMAT-PSA, Spain	Comparing direct & indirect flux measurements	sun

Continued on next page

Flux measurement activities	Published year	Research unit	Motivation	Light source
PROHERMES measures solar flux on solar tower receivers with a white rotating bar as the target and a CCD-camera taking images [7]	1999	CIEMAT-PSA, Spain	Indirect flux measurement	sun
PROHERMES used on REFOS testbed on solar tower of SSPS-CRS [8]	2000	DLR-PSA, Spain; CIEMAT-PSA, Spain	Indirect flux measurements	sun
PROHERMES used in REFOS project testing a pressurized volumetric air receiver [9]	2000	PSA, Spain	Indirect flux measurement	sun
Calibrations of PROHERMES measurement done with commercial flux gauges [10]	2004	PSA, Spain; DLR, German	Indirect flux measurements	sun
Summarized direct/indirect techniques and presented a new simulation technique [11]	2011	PSA, Spain; DLR, German	Comparing direct & indirect flux measurement	sun
PHLUX (Photographic Flux mapping) for external central receivers [12–14]	2011	SNL, USA	Indirect flux measurement	sun
Repeated PHLUX on a heliostat [15]	2015	CIOMP-CAS, China	Indirect flux measurement	sun
New flux mapping method for large receiver aperture using boundary interpolation reconstruction [16]	2011	IEE-CAS, China	Direct flux measurement	sun
Studied moonlight concentration of the solar furnace [17]	1957	NMIRI, Japan	Indirect flux measurement	full moon
Moonlight concentration on heliostats of Central-Receiver Test Facility [18]	1982	SNL, USA	Mirror canting of heliostats	full moon
Moonlight concentration performed at THEMIS solar power plant [19]	1989	PROMES, France	Evaluate optical defects of heliostat mirrors	full moon
Full moon flux mapping to characterize ANU 400 m^2 dish [20]	2004	ANU, Australia	Indirect flux measurement	full moon
Lunar flux mapping on PETAL400 m^2 dish [21]	2004	Ben-Gurion University, Israel	Indirect flux measurement	full moon
Full moon flux mapping to characterize ANU 500 m^2 dish [22]	2011	ANU, Australia	Indirect flux measurement	full moon
Moonlight concentration tests on DS1 dish [23]	2015	SOLARDIS project, Spain	Determination of optical error parameters	full moon
Full moon flux mapping at THEMIS solar power plant [24]	2013	PROMES, France	Indirect flux measurement	full moon
Moonlight concentration experiments at Badaling Solar Tower [25,26]	2019	IEECAS, China	Indirect flux measurement	full moon

To increase the usefulness of lunar flux mapping of the heliostat field, a new mechod is developed to allow more moon phases to be used. i.e. the phases between half and full moon, not only the full moon.

In this work we present a novel approach to convert lunar concentration ratio maps to a solar concentration ratio map for different moon phases/shapes. Since a solar dish and solar tower are point-focusing systems and the optical concentration of the dish concentrator is more stable and straightforward, a dish concentrator is preferable for this work. The dish can be used to investigate how the moon shapes affect the brightness distribution on the focal region of a given point-focusing solar concentrator, and the application of the method can later be extended to include lunar flux mapping of a central receiver system, and properly convert a lunar concentration ratio distribution to the corresponding solar concentration ratio distribution(CRD).

2. New lunar flux mapping model

This approach assumes that the solar/lunar CRDs of a point-focusing solar concentrator have similar distribution for the same orientation geometry of the light source and the concentrator. However, the differences are considered and recognized. Initially, we set

$$CR_{sun}(x,y) = CR_{moon}(x,y) \cdot T_1(x,y) \tag{1}$$

Here, $T_1(x,y)$ is the correction function from $CR_{moon}(x,y)$ to $CR_{sun}(x,y)$.

The cosine similarity between the solar CRD and a lunar CRD should be some function of the cosine similarity between the sun shape (solar brightness distribution) and that moon shape (noon brightness distribution). Cosine similarity is a measure of similarity between two non-zero vectors, independent of their magnitude. It is defined as the inner product of the two vectors normalized to both have length 1 [27]. We take the matrix of a concentration ratio image or the brightness distribution of the light source after discretization as a vector. Thus, the cosine similarity between the solar CRD and a lunar CRD is defined as

$$r_{cos}\big(CR_{sun}(x,y), CR_{moon}(x,y)\big) = \frac{\sum_{x,y} CR_{sun}(x,y) \cdot CR_{moon}(x,y)}{\sqrt{\sum_{x,y} CR_{sun}^2(x,y)} \cdot \sqrt{\sum_{x,y} CR_{moon}^2(x,y)}} \tag{2}$$

The cosine similarity between the sun shape and a moon shape is defined as

$$r_{cos}\big(B_{sun}(x,y), B_{moon}(x,y)\big) = \frac{\sum_{x,y} B_{sun}(x,y) \cdot B_{moon}(x,y)}{\sqrt{\sum_{x,y} B_{sun}^2(x,y)} \cdot \sqrt{\sum_{x,y} B_{moon}^2(x,y)}} \tag{3}$$

Here, $r_{cos}(CR_{sun}, CR_{moon})$ and $r_{cos}(B_{sun}, B_{moon})$ are within the range from 0 to 1.

The function relationship from the cosine similarity between light sources to the cosine similarity between the concentration ratios, derived from a well understood solar dish, is the hope of this lunar flux mapping model for a large solar tower system.

A solar tower or a solar dish as a point-focusing optical concentrator can can be treated as a an optical signal processing system. The solar flux concentration image is a transfer function of the the sun shape input . Using an input of the moon shape corresponding to different moon phases produces different lunar flux concentration images. The full moon shape is the closest to the circular symmetric sun shape. The cosine similarity between the sun shape (solar brightness distribution) and the moon shape is reduced as the fraction of moon shape is reduced. The solar concentrator has the potential to enhance the cosine similarity between the solar concentration ratio image and a lunar concentration ratio image, and the residual differences can be compensated by using a smoothing filter on the lunar concentration ratio images to approximate the solar concentration ratio image. A smoothing filter can improve the cosine similarity between the solar concentration ratio image and a lunar concentration ratio image. Thus, the smaller cosine similarity between the sun shape and the moon shape requires more smooth filtering of the lunar concentration ratio image to match the solar concentration ratio image. The principle of this flux mapping model is illustrated in Figures 1 and 2 below, which clearly shows how to convert a lunar CRD to the corresponding solar CRD for a solar concentrator by several rounds of smooth filtering.

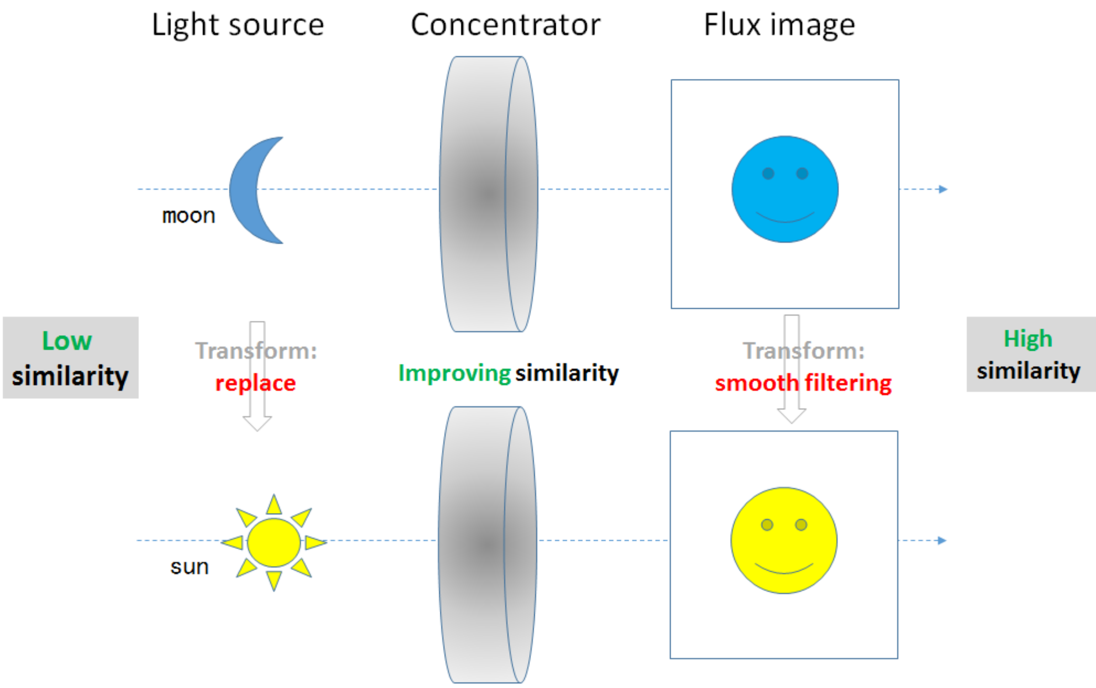

Figure 1. The principle of this lunar flux mapping model to estimate the CRD of a point-focusing solar concentrator, recognizing the potential of a solar concentrator to enhance the similarity between the solar concentration ratio image and a lunar concentration ratio image and that the residual differences can be compensated by applying a smoothing filter to a lunar concentration ratio image so that it matches the solar concentration ratio image.

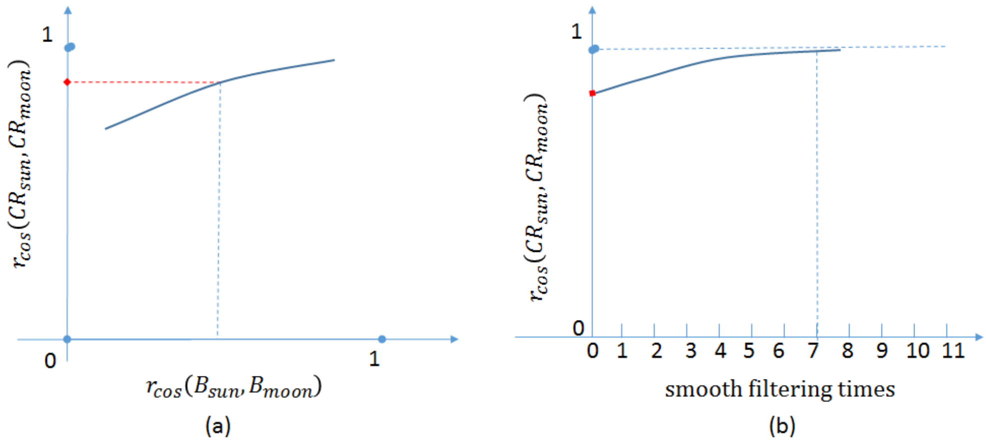

Figure 2. The principle of this lunar flux mapping model: (a) the cosine similarity between the solar concentration ratio image and a lunar concentration ratio image should be some function of the cosine similarity between the sun shape and that moon shape; (b) smoothing filtering is used to improve the cosine similarity between the solar concentration ratio image and a lunar concentration ratio image, and the times of smooth filtering is determined to approximate the cosine similarity between the solar concentration ratio image and the lunar concentration ratio image.

Since the filtering process can be expressed by convolution in mathematics, Eq (1) is rewritten as

$$CR_{sun}(x,y) = CR_{moon}(x,y) \otimes T_2(x,y) \tag{4}$$

The simplest smooth filtering of a discrete digital image uses the 3 × 3 mask of average filter,

$$M = \begin{bmatrix} 1 & 1 & 1 \\ 1 & 1 & 1 \\ 1 & 1 & 1 \end{bmatrix} / 9,$$

i.e.,

$CR_{moon}(x,y) \otimes M = [CR_{moon}(x - \triangle, y - \triangle) + CR_{moon}(x, y - \triangle) + CR_{moon}(x + \triangle, y - \triangle) + CR_{moon}(x - \triangle, y) + CR_{moon}(x,y) + CR_{moon}(x + \triangle, y) + CR_{moon}(x - \triangle, y + \triangle) + CR_{moon}(x, y + \triangle) + CR_{moon}]/9.$

Here $\triangle$ is the pixel size of the image $CR_{moon}(x,y)$. Two times of smooth filter is

$$T(2) = M \otimes M$$

and N times of smoothing filter is expressed as

$$T(N) = \underbrace{M \otimes M \otimes \cdots M}_{N}.$$

Thus, based on Eq (4), N times of smoothing filtering of a digital lunar concentration ratio image to approximate the solar concentration ratio image can be rewritten as

$$CR_{sun}(x,y) = c \cdot CR_{moon}(x,y) \otimes T(N) \tag{5}$$

Here, the coefficient c is a scalar reserved for the final modulation of the smoothed concentration ratio image. Equation (5) is an excellent approximative solution of Eq (1) regarding the transfer function $T_1(x,y)$ and the $T_1(x,y)$ is specified as the combination form of scalar c and digital convolution operations.

3. Ray tracing for simulation of solar/lunar CR distribution

3.1. Backward ray tracing with effective moon shapes

The authors previous work shows the geometry and the formula for calculating concentrated solar flux density using backward ray tracing (BRT) with effective circular symmetric sun shape [29]. The backward ray tracing is modified with effective sun/moon shapes to simulate the concentration ratio distribution. The effective moon shape, or brightness distribution, is the convolution of the actual moon shape and the mirror optical errors. This optical simulation method is generalized for various circular and noncircular moon shapes. The brightness distribution of the moon is normalized to one for integration.

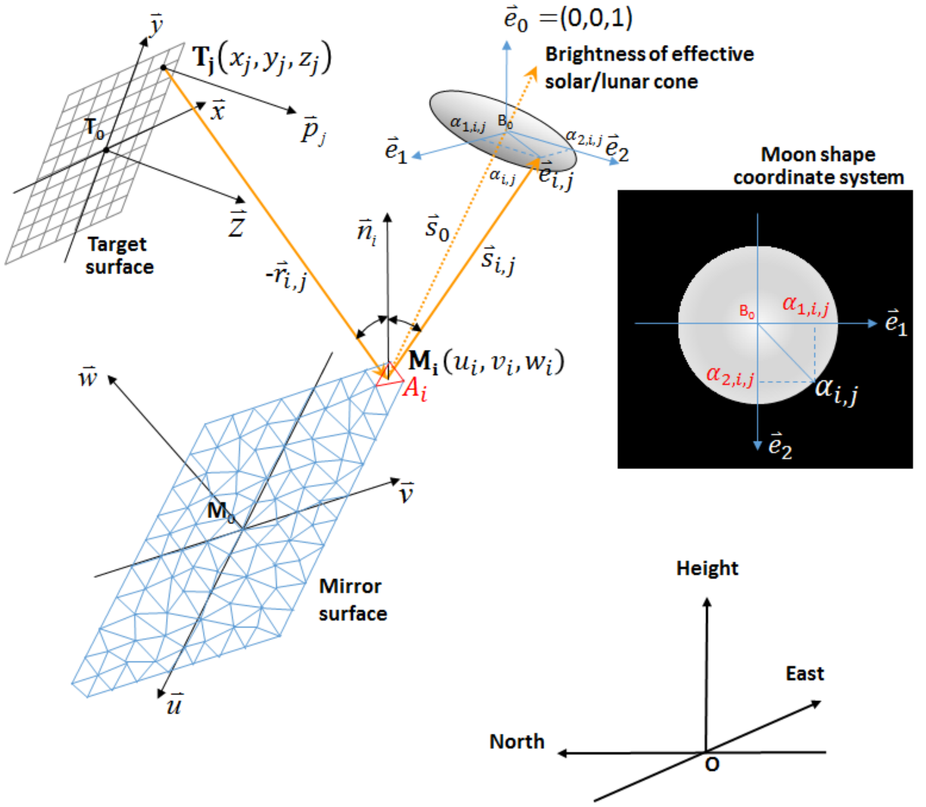

Figure 3. The geometry and principle of the BRT with effective moon shapes, target surface gridding, and the arbitrary mirror surface meshing for simulation of CRD on the target surface.

In Figure 3, [O, North, East, Height] is the global coordinate system, $\vec{s}_0$ is the unit light source vector, $\vec{z}$ is the target plane normal at the target center T_0, (x_j, y_j, z_j) are the coordinates of point T_j

in the target coordinate system [T₀, $\vec{x}$,$\vec{y}$,$\vec{z}$], $\vec{p}_j$ is the normal vector of the target surface at T_j, (u_i, v_i, w_i) are the coordinates of the center point M_i of the i^{th} mirror surface element in the mirror surface coordinate system [M_0,$\vec{u}$,$\vec{v}$,$\vec{w}$], $\vec{n}_i$ is the mirror surface normal at the i^{th} mirror point M_i, -$\vec{r}_{i,j}$ is the unit vector of the backward ray from target point T_j to mirror point M_i, $\vec{s}_{i,j}$ is the reflection unit vector for -$\vec{r}_{i,j}$ after being reflected at point M_i; the two-dimensional brightness distribution of the effective moon can be denoted as $\phi_{eff}(\alpha_1, \alpha_2)$ with the unit of 1/(m^2·sr) and the integration of $\phi_{eff}(\alpha_1, \alpha_2)$ over the full solid angle equals 1/m^2. α_1 and α_2 are the angular parameters for the moon shape, and B_0 denotes the moon center. [B_0,$\vec{e}_1$,$\vec{e}_2$] is the plane coordinate system for the moon shape and [B_0,$\vec{e}_1$,$\vec{e}_2$, $-\vec{s}_0$] forms a left-handed three-dimensional Cartesian coordinate system. α is the radial angular parameter of the moon image with $\alpha = \sqrt{\alpha_1^2 + \alpha_2^2}$. $\vec{e}_{i,j}$ is the projection vector of $\vec{s}_{i,j}$ in the plane of [B_0,$\vec{e}_1$,$\vec{e}_2$] and $\cos(\alpha_{i,j}) = (\vec{s}_{i,j} \cdot \vec{s}_0)$.

The area of the i^{th} mirror surface element is denoted as A_i and $L_{i,j}$ is the slant distance from point T_j (x_j, y_j, z_j) to point $M_i(u_i, v_i, w_i)$. Following the denotations in Figure 3, the concentration ratio distribution, $CR_{moon}(x_j, y_j)$, at the target surface point at T_j is numerically calculated as Eq (6).

$$\begin{cases} CR_{moon}(x_j, y_j) = \sum_{i=1}^{I} \rho_{m,i} \cdot \tau_j \cdot U(-\vec{r}_{i,j} \cdot \vec{p}_j) \cdot (-\vec{r}_{i,j} \cdot \vec{p}_j) \cdot (\vec{r}_{i,j} \cdot \vec{n}_i) \frac{A_i}{L_{i,j}^2} \phi_{eff}(\alpha_{1,i,j}, \alpha_{2,i,j}) \\ U(\lambda) = \begin{cases} 1, if\ \lambda > 0 \\ 0, if\ \lambda \le 0 \end{cases} \\ \alpha_{1,i,j} = \vec{e}_1 \cdot \vec{e}_{i,j}, \alpha_{2,i,j} = \vec{e}_2 \cdot \vec{e}_{i,j}, \vec{e}_{i,j} = \vec{s}_{i,j} - \vec{s}_0(\vec{s}_{i,j} \cdot \vec{s}_0) \\ \vec{e}_1 = (\vec{e}_0 \times \vec{s}_0)/\|\vec{e}_0 \times \vec{s}_0\|_2, \vec{e}_2 = \vec{e}_1 \times \vec{s}_0, \vec{s}_{i,j} = 2(\vec{r}_{i,j} \cdot \vec{n}_i)\vec{n}_i - \vec{r}_{i,j} \end{cases} \quad (6)$$

Here, $\rho_{m,i}$ is the specular reflectance of the i^{th} mirror surface element, and τ_j is the transmittance of the receiving surface at T_j. τ_j = 1, when the target plane has no window cover.

For a dual-axis tracking solar dish concentrator, it should be: $\vec{s}_0 = \vec{w} = -\vec{z}$, which means the dish concentrator is directly facing, and the target plane is exactly back facing to the sun or the moon.

For BRT with an effective moon shape, bundles of rays are fired at each target point of interest, strike directly at all the geometric centers of the mirror elements of the meshed mirror surface, are then backwardly reflected into the effective moon cone centered around the moon vector. All the optical errors are convoluted into the effective moon cone. The total optical error cone is here supposed to be circular Gaussian type (normal distribution).

3.2. Discrete effective moon shapes

Normalized discrete moon-shapes, $\phi_{moon}(\alpha_{1,i}, \alpha_{2,j})$, are created by using a CCD camera to capture various moon images at night, digitally processing to find out the moon centers and the gray centroids in the pictures and the pixel widths, and saving the the greyscale moon images as numerical matrices. The discrete moon-shapes are normalized, i.e.,

$$1 = \sum_{i=1,2,\cdots,Ni; j=1,2,\cdots,Nj} \phi_{moon}(\alpha_{1,i}, \alpha_{2,j}).$$

Figure 4 shows an un-normalized digital moon image to be used as the discrete moon shape, with the pixel width $\mathrm{dp} = 4.5588 \times 10^{-2}$ mrad and image size $Nj = Ni = 1025$. Figure 11(b) shows the horizontal and vertical profiles of the effective moon shape passing through the image center (centroid). The biases of the image center (centroid) of this half-moon shape from the reference moon disk center are −0.4559 mrad in horizontal α_1 direction and 2.5529 mrad in vertical α_2 direction. This bias is equivalent to some tracking error and affects the lunar concentration distribution, so it should be considered carefully.

With the same pixel width dp and size ($Nj \times Ni$) of the moon image, given the sigma value of the circular Gaussian distribution, the discrete optical error cone is normalized and formulated as Eq (7) below. Based on Eq (7) and corresponding to the size of the moon shape image in Figure 4, Figure 5 shows the normalized discrete circular Gaussian distribution of the total optical error cone, with the sigma parameter of σ_{err} = 0.5 mrad.

$$\begin{cases} \phi_{err}(\alpha_{1,i}, \alpha_{2,j}) = exp\left(-\frac{\alpha_{1,i}^2+\alpha_{2,j}^2}{2\sigma_{err}^2}\right)/W_{err} \\ W_{err} = \sum_{i=1,2,\cdots,Ni;j=1,2,\cdots,Nj} exp\left(-\frac{\alpha_{1,i}^2+\alpha_{2,j}^2}{2\sigma_{err}^2}\right) \\ \alpha_{1,i} = dp \cdot \left(i - \frac{Ni+1}{2}\right), \alpha_{2,j} = dp \cdot \left(j - \frac{Nj+1}{2}\right) \end{cases} \tag{7}$$

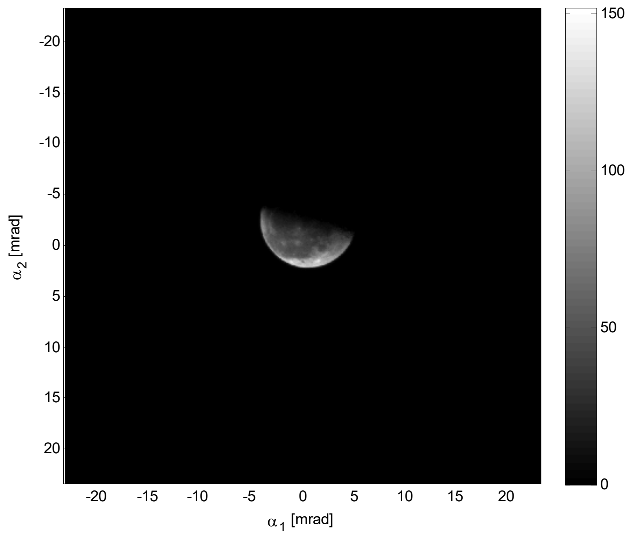

Figure 4. The grayscale moon image by a CCD camera with a telephoto lens is processed and then used as a Last Quarter moon shape model (not normalized yet) for the light source.

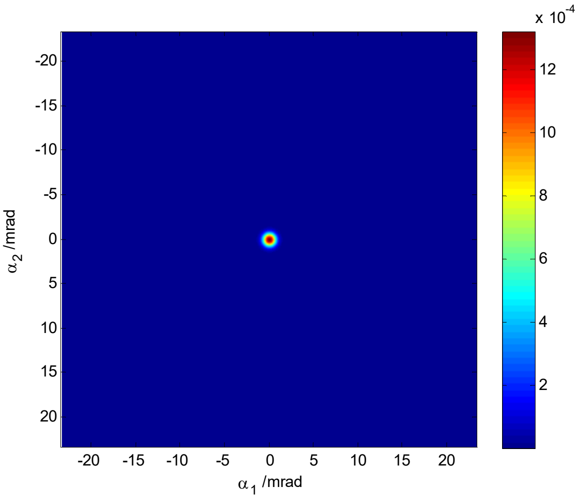

Figure 5. Normalized discrete optical error shape in a circular Gaussian distribution with σ_{err} = 0.5 mrad.

A discrete effective moon shape is easily derived by two-dimensional convolution of the moon shape image and the normalized error image using digital image processing methods, such as digital filter, discrete convolution, and Fast Fourier Transform (FFT). The computation algorithm for the normalized discrete effective moon shape is given below as Eq (8). The FFT of the two images can implement the discrete convolution of two digital images and then the inverse FFT (IFFT) of the product of FFT results.

$$\begin{aligned}\{\phi_{eff}(\alpha_{1,i},\alpha_{2,j})\}_{i=1,2,\cdots,Ni}^{j=1,2,\cdots,Nj} &= \{\phi_{moon}(\alpha_{1,i},\alpha_{2,j})\}_{i=1,2,\cdots,Ni}^{j=1,2,\cdots,Nj} \otimes \{\phi_{err}(\alpha_{1,i},\alpha_{2,j})\}_{i=1,2,\cdots,Ni}^{j=1,2,\cdots,Nj} \\ &= IFFT\left(FFT\left(\{\phi_{moon}(\alpha_{1,i},\alpha_{2,j})\}_{i=1,2,\cdots,Ni}^{j=1,2,\cdots,Nj}\right) \cdot FFT\left(\{\phi_{err}(\alpha_{1,i},\alpha_{2,j})\}_{i=1,2,\cdots,Ni}^{j=1,2,\cdots,Nj}\right)\right)\end{aligned} \tag{8}$$

The derived discrete effective moon shapes are used of lunar CR distribution on the target plane of a solar concentrator.

Based on Eq (8) and corresponding to Figures 4 and 5, Figure 6 shows the resulting discrete effective moon shape (not normalized yet).

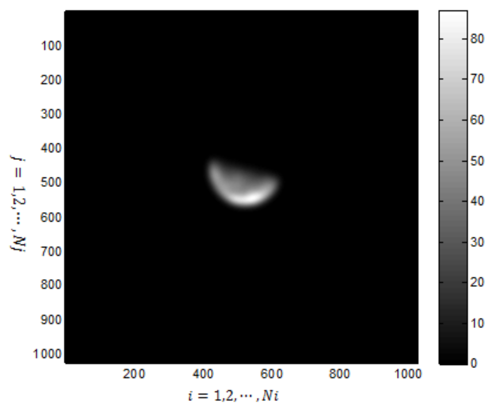

Figure 6. The discrete effective moon shape (not normalized yet) with the pixel width $\mathrm{dp} = 4.5588 \times 10^{-2}$ and image size $Nj = Ni = 1025$.

For general implemention of this BRT method with practical considerations, an effective moon shape is discretely modeled as a matrix instead of an analytic function of two variables, and the brightness value of $\phi_{eff}(\alpha_1, \alpha_2)$ at the variable values of (α_1, α_2) is determined by some two-dimensional interpolation from the discrete values $\phi_{eff}(\alpha_{1,i}, \alpha_{2,j}), i = 1,2,\cdots, Ni, j = 1,2,\cdots, Nj$. The discrete effective-moon-shapes are normalized, i.e.,

$$1 = \sum_{i=1,2,\cdots,Ni;j=1,2,\cdots,Nj} \phi_{eff}(\alpha_{1,i}, \alpha_{2,j}).$$

4. The solar dish concentrator and moonlight concentration experiments

4.1. The solar dish concentrator and the experimental setup

A parabolic solar dish concentrator was constructed in the heliostat field of the 1MW Badaling solar tower power plant in Beijing, as shown in Figure 7. The outer diameter of the dish aperture is about 3 m, the inner diameter is about 0.3 m, and its focal length is about 1.55 m. The concentrator comprises 18 mirror facets in two rings, six facets for the inner ring, and 12 facets for the outer ring, and the total mirror surface area is about 6.653 m^2.

Figure 7. The experimental parabolic solar dish concentrator in Beijing.

The compound mirror surface of the dish concentrator was surveyed using a 3D laser scanner with diffuse-reflective contrast power uniformly sprayed on the mirrors. As Figure 8 shows, the scanned point cloud data of the mirror surface was edited by the free code MeshLab, a 3D mesh processing software system. The uniform triangular mesh was generated for each mirror facet to use the BRT with effective moon shapes. To adequately represent the profile shape of the entire mirror surface, the area of each mirror surface element is about six mm^2. The coordinates of the center of each mirror surface element are taken as the centroid of the three corner nodes, i.e., the mirror element center is calculated as the arithmetic mean of the three triangle corners. The normal vector of the mirror element at the mirror element center is expressed as the plane normal of the triangle.

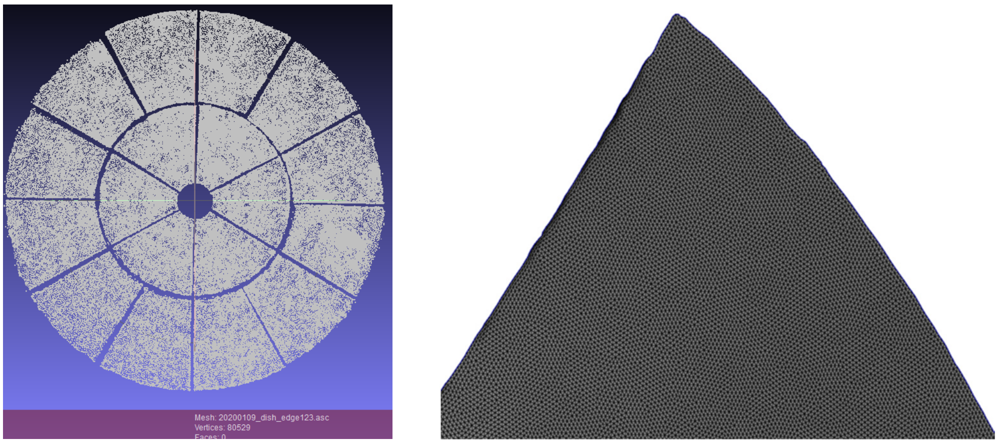

(a) (b)

Figure 8. Onsite laser-scanned 3D point-cloud-data of mirror surface viewed and edited by MeshLab; (a) plan view of the point cloud data after data trimming; (b) uniform triangle mesh of a mirror facet after interpolation-resampling the mirror surface data.

A solar dish concentrator is naturally a dual-axis sun/moon tracker. For measuring the lunar CRD on the target plane, the moonlight concentration test setup was built with some critical measuring components, such as the reference weak-light illuminometer for measuring DNI_{moon}, a CCD camera with a telephoto lens for taking images of the moon in the sky, a sandwich-type target complex, and a short focal length CCD camera for taking the concentrated lunar images on the white front target, as Figure 9 shows. The sandwich-type target complex comprises the front diffuse-reflective circular white target, six illuminometers in the middle layer, and the rear metal disk. The six illuminometers are behind the six holes of the front target disk and fixed on the rear metal disk, and the rear metal disk is mounted on the receiver supporting structure of the concentrator. The optical axis of the concentrator connects the dish center and the target center, which is a reference line to align all the measuring components. A hard paper tube was used on the reference illuminometer probe to avoid the stray light and scattered light from the sky and the ambient.

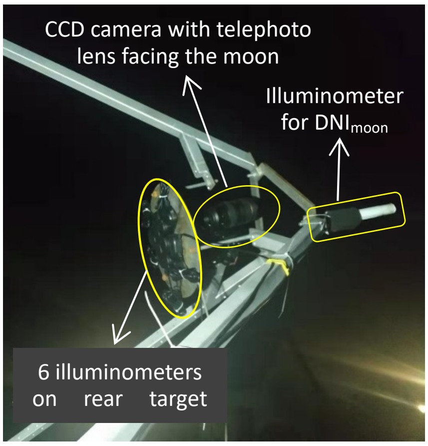

(a)

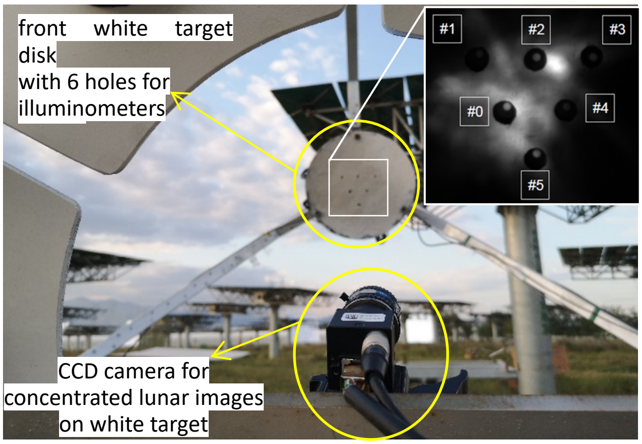

(b)

Figure 9. The moonlight concentration test setup on the dish concentrator with all the measuring components being aligned along the axis of the concentrator; (a) a reference illuminometer covered with a hard paper tube for measuring the direct normal illuminance of the moonlight and a CCD camera with a telephoto lens was mounted on the receiver supporting structure, and six illuminometers were compactly fixed on the rear metal disk of the sandwich-like target complex before the front covering white target disk being installed; (b) a short focal length CCD camera was mounted on the central frame of the concentrator, facing the white target disk which has six holes made for the six illuminometers behind.

4.2. The experimental results

Figure 4 above shows a Last Quarter moon image from the long-focal-length CCD camera to be used as the discrete moon shape model, with the pixel width $dp = 4.5588 \times 10^{-2}$ mrad and image size $Nj = Ni = 1025$. The original half-moon image was taken on Sept. 21st, 2019. Figure 6 shows the resulting discrete effective half-moon for the circular Gaussian error with the sigma parameter value of 0.5 mrad. Similarly, Figure 10 shows a Waning Gibbous moon image from the long-focal-length CCD camera used as the discrete moon shape. The original Waning Gibbous moon image was taken on Sept. 17th, 2019. Figure 11 shows the resulting discrete effective Waning Gibbous moon shape (not normalized yet) with the same pixel width and image size. Figure 11(a) is for the image of the effective Waning Gibbous moon shape, and Figure 11(b) especially shows the horizontal and vertical profiles of the effective moon shape across through the image center (centroid). Referencing to the moon disk center, the center of this Waning Gibbous moon shape (image center) biases for −0.4103 mrad in horizontal α_1 direction and 0.7750 mrad in vertical α_2 direction. This bias of the image centroid from the moon disk center is equivalent to some tracking error of the solar dish, which affects the lunar concentration image, so it should be considered seriously.

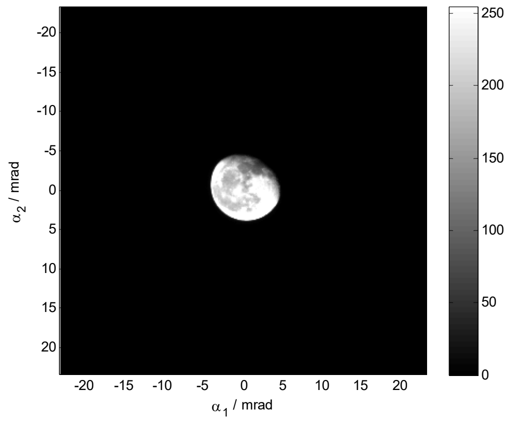

Figure 10. The gray-value moon image by a CCD camera with a telephoto lens is processed and then used as a Waning Gibbous moon shape model (not normalized yet).

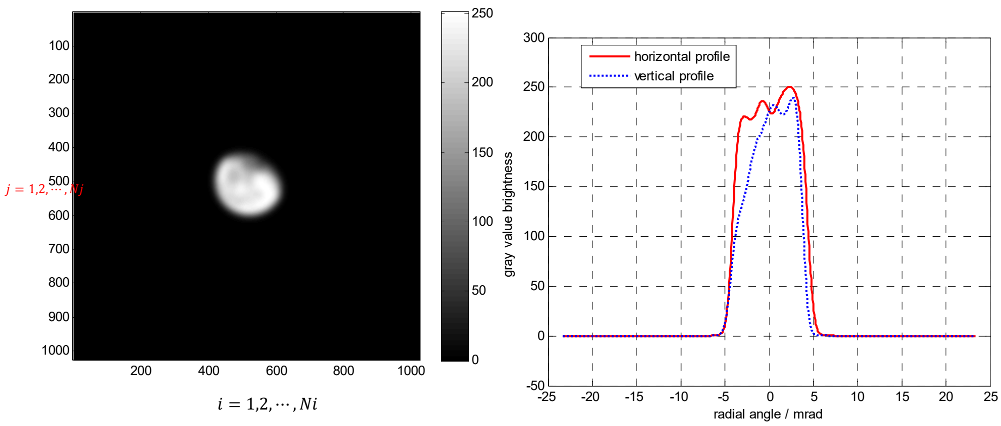

(a) (b)

Figure 11. The discrete effective Waning Gibbous moon shape (not normalized yet) with the pixel width $\mathrm{dp} = 4.5588 \times 10^{-2}$ mrad and image size $Nj = Ni = 1025$; (a) image of an effective Waning Gibbous moon shape; (b) the horizontal and vertical profiles of the effective moon shape across through the gray-value centroid.

Two typical moonlight concentration images of the dish concentrator were recorded by the short focal length CCD camera in front of the white target disk for the Waning Gibbous moon shape in Figure 10 and the Last Quarter moon shape in Figure 4, respectively. The concentrated lunar image in Figure 12(a) for the Waning Gibbous moon is naturally brighter than the image in Figure 12(b) for the half-moon, thanks to the difference of the $\mathrm{DNI}_{\mathrm{moon}}$. In contrast, their normalized concentration lunar images are similar.

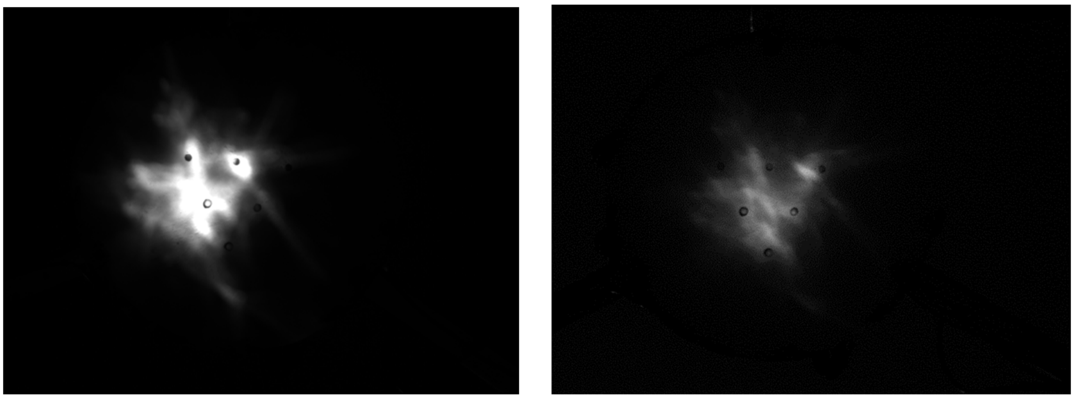

(a) (b)

Figure 12. Two typical moonlight concentration images on the white target disk: (a) taken on Sept. 17th, 2019 for the Waning Gibbous moon shape in Figure 10; (b) taken on Sept. 21st, 2019 for the Last Quarter moon shape in Figure 4.

4.3. Simulation of concentrated lunar images to match the experimental images

Based on similarities of the contours and shapes of the concentrated lunar images, the parametric values of the focal length of the solar dish and the sigma of the circular Gaussian error cone are adjusted and determined for the BRT optical simulation model for the concentration ratio distribution (CRD). Hence, the focal length of the solar dish is figured out as f = 1.55 m (see Figure 7), and the optical error parameter σ_{err} = 0.5 mrad (see Figure 5).

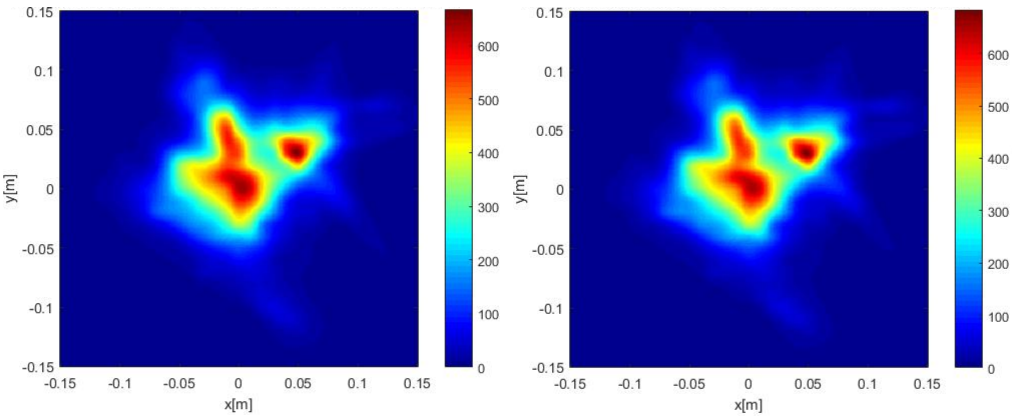

(a) (b)

Figure 13. Simulated lunar CRD images respecting the two typical moon shapes: (a) CRD image for the Waning Gibbous moon shape in Figure 10; (b) CRD image for the Last Quarter moon shape in Figure 4.

Regarding the Waning Gibbous moon shape in Figure 10, Figure 13(a) shows the simulation of the CRD image of the solar dish using the BRT with discrete effective moon shape (see Figure 11). Regarding the half moon shape in Figure 4, Figure 13(b) shows the simulation of the CRD. In the optical simulations using Eq (6), $\rho_{m,i}$ is set as 0.85, τ_j = 1. The peak value of CRD in Figure 13(a) is 659.13, and the peak value of CRD in Figure 13(b) is 685.68. Figure 13(a) and (b) clearly show the similarity of the shapes of the lunar concentration images. The peak value of CRD in Figure 13(b) for the half moon shape is slightly higher than that of CRD in Figure 13(a) due to the more prominent brightness non-uniformity of the smaller half-moon.

In the simulations, the uniform sampling steps in the x and y directions in the target plane are set as $\triangle_x = 0.01$ m and $\triangle_y = 0.01$ m, number of sampling rows is $N_y = 31$, number of sampling columns is $N_x = 31$, the target size is

$$T_x \times T_y = [(N_x - 1)\triangle_x] \times [(N_y - 1)\triangle_y] = 0.30 \text{ m} \times 0.30 \text{ m},$$

$$x_j \in [-\tfrac{N_x-1}{2}, \cdots, -1, 0, 1, \cdots, \tfrac{N_x-1}{2}] \times \triangle_x,$$

$$y_j \in [-\tfrac{N_y-1}{2}, \cdots, -1, 0, 1, \cdots, \tfrac{N_y-1}{2}] \times \triangle_y, j = 1, 2, \cdots, N_x \times N_y.$$

The computed CR values matrix is finally refined into the lunar CRD image by two-dimensional interpolation with the pixel size $\triangle = 0.001$ m, so the final image size is 301 × 301.

5. Converting a lunar CRD to the solar CRD

Figures 1 and 2 show how to convert a lunar CRD to the corresponding solar CRD. Here, we try to convert the two typical simulated lunar CRD images shown in Figure 13 to the expected solar CRD image of the dish concentrator.

5.1. Simulation of the solar CRD image

Before converting a lunar CRD to the solar CRD, the expected solar CRD should be simulated using the BRT with discrete effective sun shape with the same parameter settings. One of the most realistic sun shape models is the Buie sun shape [28], which adopts the circumsolar ratio (CSR) parameter to consider the limb-darkened solar disk with circumsolar radiation. Thus, Buie sun shape is adopted to simulate the solar CRD image, though Pillbox (uniform) and Gaussian sun shapes are also commonly used in solar engineering modeling. Similar to the discrete effective moon shape created in Figure 11, a discrete effective sun shape image is developed after two-dimensional convolution of the discrete Buie sun shape image with the normalized Gaussian error image.

Figure 14 shows the discrete circular-symmetric Buie sun shape with pixel width $\text{dp} = 4.5588 \times 10^{-2}$ mrad and image size $Nj = Ni = 102$. Figure 15 shows the developed circular-symmetric effective Buie sun shape image for CSR = 0.1 and σ_{err} = 0.5 mrad.

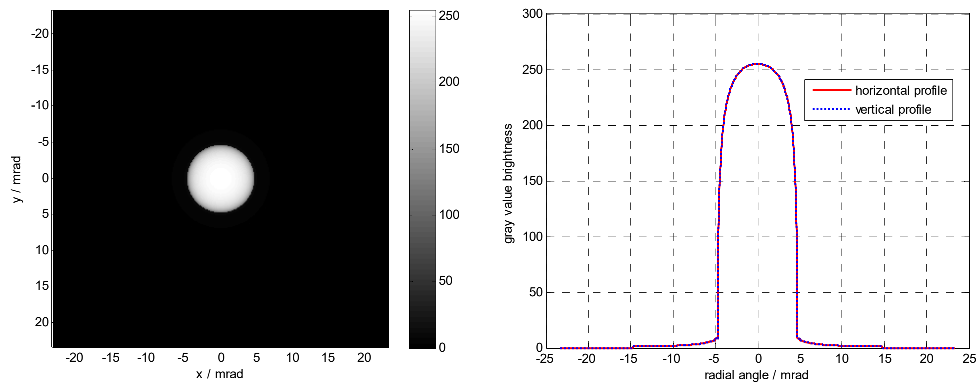

(a) (b)

Figure 14. The discrete Buie's sun shape (not normalized yet) for CSR = 0.1, pixel width $\mathrm{dp} = 4.5588 \times 10^{-2}$ mrad and image size $Nj = Ni = 1025$; (a) sun shape image; (b) the horizontal and vertical profiles across through the image center.

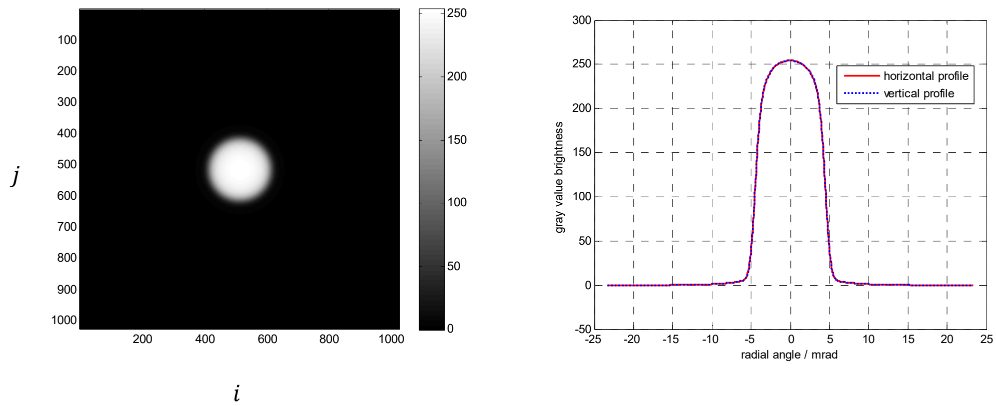

(a) (b)

Figure 15. The discrete effective sun shape (not normalized yet) with the pixel width $\mathrm{dp} = 4.5588 \times 10^{-2}$ mrad and image size $Nj = Ni = 1025$; (a) effective sun shape image; (b) the horizontal and vertical profiles across through the image center.

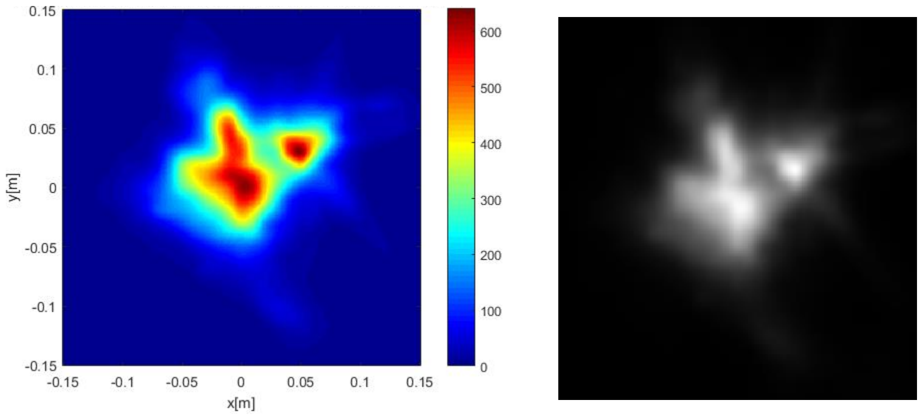

(a) (b)

Figure 16. Simulated solar CRD respecting Buie sun shape with CSR = 0.1: (a) color image with color bar and dimensions; (b) naked grayscale image.

For the Buie sun shape shown in Figure 14 and the discrete effective sun shape shown in Figure 15, Figure 16 shows the simulated solar CRD image of the dish concentrator using Eq (6). In the optical simulation, $\rho_{m,i}$ is 0.85, τ_j = 1. The peak value of solar CRD in Figure 16(a) is 641.22, which is smaller than those peak values of lunar CRD in Figure 13(a) and Figure 13(b). The lowest peak value of simulated solar CRD is due to the sun shape's most uniform and circular-symmetric feature compared with the moon shapes.

5.2. Comparing moon shapes to the sun shape

After analysis by Eq (3), the cosine similarity between the sun shape (Figure 14) and the Waning Gibbous moon shape (Figure 10) is $r_{cos}(B_{sun}, B_{moon1})$ = 0.9279, and the cosine similarity between the sun shape (Figure 14) and the half-moon shape (Figure 4) is $r_{cos}(B_{sun}, B_{moon2})$ = 0.6687. The cosine similarity $r_{cos}(B_{sun}, B_{moon2})$ is 0.2592 less than $r_{cos}(B_{sun}, B_{moon1})$, which indicates that the similarity of the moon 1 (a Waning Gibbous moon) to the sun is better than the moon 2 (Last Quarter).

Figure 17 shows the radial density distributions of the two typical moon shapes and the Buie sun shape. Referencing the modeled sun shape, Figure 17(a) compares shapes of the moon 1 and the sun, and Figure 17(b) compares shapes of the moon 2 and the sun. Calculation of the radial density distribution of a two-dimensional distribution image (sun shape or moon shape) is conducted using the numerical method presented in detail by the authors [16].

For example, the radial density distribution of a bivariate normal distribution is the Rayleigh distribution with the same 'sigma' value. The circumferential density distribution is uniform over the angular range of [0, 2π]. Figure 17(a) and (b) clearly show again that the similarity of moon 1 to the sun is better than moon 2.

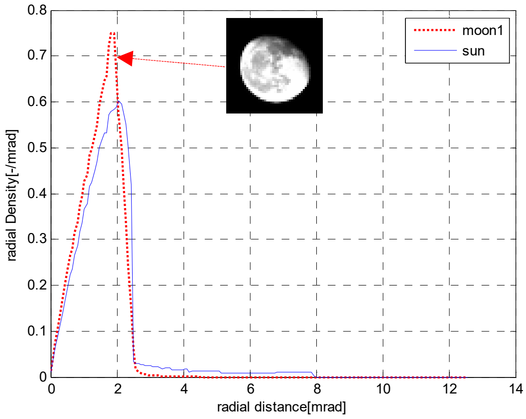

(a)

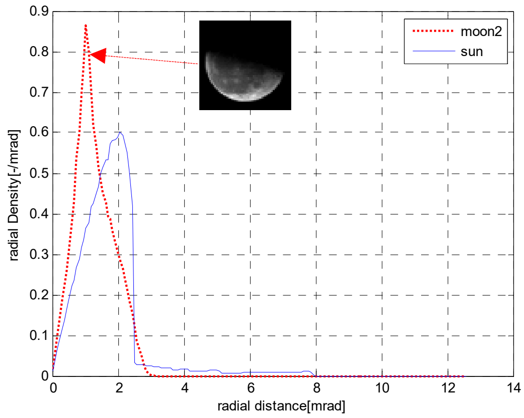

(b)

Figure 17. Radial density distribution of the modeled moon shapes and the sun shape: (a) Waning Gibbous moon and the sun; (b) Last Quarter moon and the sun.

5.3. *Comparing lunar CRD images to solar CRD image*

The two zoom-in graphs of Figure 18 show the radial density distributions of the two simulated lunar CRD images before smooth-filtering and the solar CRD image. Referencing the expected solar CRD (Figure 16(a)), Figure 18(a) compares CRD images of moon 1 and the sun, and Figure 18(b) compares CRD images of the moon 2 and the sun. The closing curves of the radial density distributions in Figure 18(a) and (b) show clearly the good similarity of CRD images for different sun shape and moon shapes. However, there are some subtle differences between the two radial density distributions of lunar CRD referencing solar CRD.

After analysis by Eq (2), the cosine similarity between the solar CRD (Figure 16(a)) and the CRD for the moon 1 (Figure 13(a)) is $r_{cos}(CR_{sun}, CR_{moon1}) = 0.99985$, and the cosine similarity between the solar CRD (Figure 16(a)) and the CRD for the moon 2 (Figure 13(b)) is $r_{cos}(CR_{sun}, CR_{moon2}) = 0.99960$. The cosine similarity $r_{cos}(CR_{sun}, CR_{moon2})$ is 0.00025 less than $r_{cos}(CR_{sun}, CR_{moon1})$. And this relatively small difference indicates the good similarity of CRD images again, and the solar dish concentrator has the potential to enhance the similarity of CRD images for different sun shape and moon shapes.

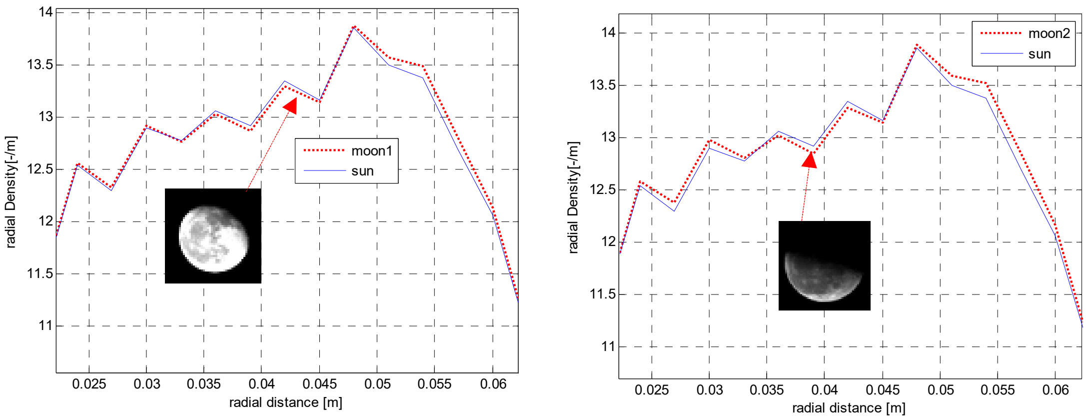

(a) (b)

Figure 18. Comparison of radial density distributions of the CRD images for different moon shapes and the sun shape: (a) for the Waning Gibbous moon and the sun; (b) for the Last Quarter moon and the sun.

5.4. Converting lunar CRD images to solar CRD image

The contours and shapes of the lunar CRD images in Figure 13(a) and (b) are quite similar to the solar CRD image in Figure 16(a), which gives us helpful information. Thus, we are inspired to compensate for residual differences by applying the smoothing filtering technique on a lunar concentration ratio image to approximate the expected solar concentration ratio image, as Figure 1 illustrates.

Figure 19(a) shows the approximative CRD image to the solar CRD after appling a smoothing filter six times to the CRD image of the moon 1, using Eq (5). In the zoom-in graph of Figure 19(b), the radial density distributions of the approximative CRD and the solar CRD are compared. The peak value of the approximative CRD in Figure 19(a) is 648.09, which is between the peak value of CRD of the moon 1 (659.13) and that of the solar CRD (641.22). The cosine similarity between the solar CRD (Figure 16(a)) and the approximative CRD for the moon 1 (Figure 19(a)) is $r_{cos}\left(CR_{sun}, CR_{appr1}\right) = 0.99995$, which is close to 1 and 0.00010 higher than $r_{cos}(CR_{sun}, CR_{moon1})$.

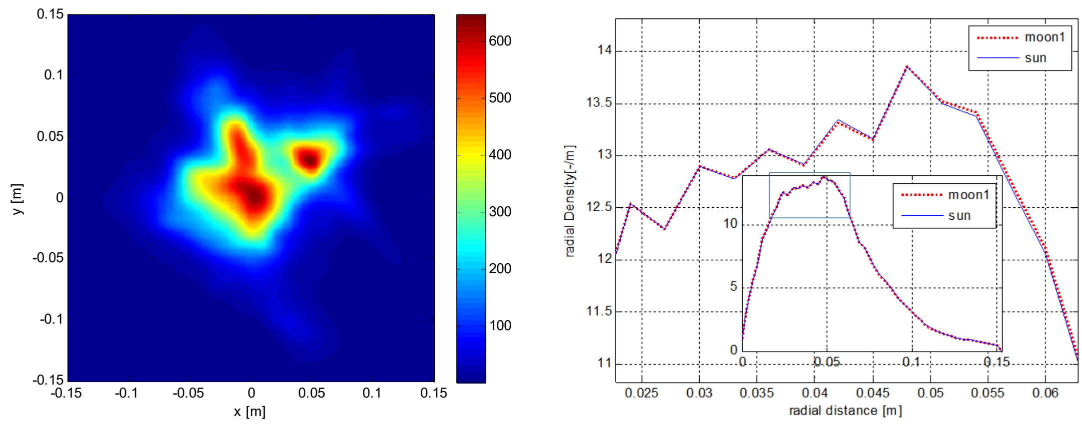

(a) (b)

Figure 19. The approximative CRD to the solar CRD after applying a smoothing filter six times to CRD of the moon 1: (a) CRD image after smooth-filtering; (b) comparison of radial density distributions of the smoothed CRD and the solar CRD.

Figure 20(a) shows the approximative CRD image to the solar CRD after applying the smoothing filter 15 times to the CRD image of the moon 2, using Eq (5). In the zoom-in graph of Figure 20(b), the radial density distributions of the approximative CRD and the solar CRD are compared.

The peak value of the approximative CRD in Figure 20(a) is 636.89, which is a little less than and close to that of the solar CRD (641.22). The cosine similarity between the solar CRD (Figure 16(a)) and the approximative CRD related to the moon 2 (Figure 20(a)) is $r_{cos}\left(CR_{sun}, CR_{appr2}\right)$ = 0.99989, which is close to 1 and 0.00029 higher than $r_{cos}(CR_{sun}, CR_{moon2})$.

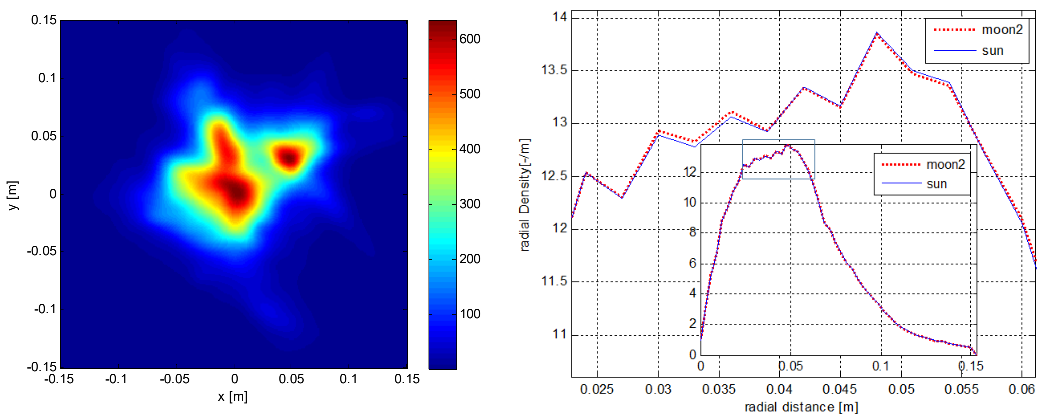

(a) (b)

Figure 20. The approximative CRD to the solar CRD after applying the smoothing filter 15 times to the CRD of the moon 1: (a) CRD image after smooth-filtering; (b) comparison of radial density distributions of the smoothed CRD and the solar CRD.

6. Discussion

The backward ray tracing (BRT) with effective sun/moon shapes for simulation of dimensionless CRD is developed from the BRT with effective round sun shape [27] for simulation of the concentrated solar flux density distribution (in kW/m^2) of a solar concentrator. Here, the effective moon shape with the unit of 1/(m^2·sr), $\phi_{eff}(\alpha_1, \alpha_2)$, is normalized to one as for the integration, i.e., the integration of $\phi_{eff}(\alpha_1, \alpha_2)$ over the full solid angle equals 1 with the unit of 1/m^2. However, in the original BRT with an effective round sun shape (solar cone brightness distribution), the effective sun shape is denoted as $\phi_{eff}(\alpha)$, with the unit of kW/(m^2·sr), its integration over the full solid angle is equal to DNIsun with the unit of kW/m^2. That is to say, the value of DNIsun is contained in $\phi_{eff}(\alpha)$ for simulation of solar flux density distribution, while $\phi_{eff}(\alpha_1, \alpha_2)$ for simulation of CRD has no information of DNIsun or DNImoon, or equivalently DNI = 1 for CRD simulations.

In this paper, Buie's sun shape is adopted among the common sun shapes to develop the discrete effective sun shape and then simulate the solar CRD image. The uniform sun shape and the normal sun shape result in similar CRD images of the dish concentrator from the additional optical simulations beyond this paper. The good similarities of the lunar CRD images show the subtle effects of light source shapes on the CRD of a point-focusing solar concentrator.

One approximative CRD to the solar CRD is developed from the CRD of the moon 1 (Waning Gibbous moon shape with the bigger phase of the moon) by apppling a smoothing filter 6 times (see Figure 19), and another approximative CRD to the solar CRD is developed from the CRD of the moon 2 (Last Quarter moon shape with the smaller phase of the moon) through applying a smoothing filter 15 times (see Figure 20). More smooth-filtering operations are needed to enhance the approximative CRD respecting the lower cosine similarity between the sun shape and the moon shape. Both approximative CRD images have better similarities to the solar CRD after the smooth-filtering operations and their cosine similarities, $r_{cos}(CR_{sun}, CR_{appr1})$ and $r_{cos}(CR_{sun}, CR_{appr2})$, are tightly close to 1.

In this paper, we present a lunar flux preliminary mapping model to better estimate the expected solar CRD by smooth-filtering operations and without providing an exact criterion to determine the number N of smooth-filtering operations. However, it is clear that N increases when the moon phase decreases and that the moon phase determines N. It is expected that the cosine similarity between the solar CRD and the approximative CRD after smooth-filtering is tightly close to 1 and greater than 0.9998. Generally, the more convolutions are performed, the more bias errors of the effective sun/moon shapes are created. Convolution operators tend to transform and enlarge the model of a moon shape into a Gaussian function. Excessive smooth-filtering of the lunar CRD may result in distortions of the approximative CRD and deviation of the approximative CRD from the expected solar CRD. Clearly, a rational tradeoff is necessary between over-filtering and the high similarity of approximative CRD to the solar CRD. The filtering number N should be as small as possible. A criterion for N should be presented in future work.

These two operational examples successfully illustrate how to convert a lunar CRD to the corresponding solar CRD for a dish solar concentrator, following the principle of this new lunar flux mapping model for a solar concentrator illustrated in Figures 1 and 2.

In the view of an optical image processing system, the output CRD of the point-focusing concentrator at a given working state should be entirely determined by the input of sun shape or moon shape, so the difference between the CRD images is also wholly determined by the difference between the sun or moon shapes. The cosine similarity is the critical metric index for analyzing and comparing the sun/moon shapes and the solar/lunar CRD images. The smooth-filtering operator of the digital images is crucial to map a lunar CRD to the expected solar CRD.

Although both approximate CRD images have good similarities to the solar CRD image, the peak values of the two approximative CRD images are still slightly different from the peak value of the solar CRD. It should be noted that the cosine similarity is independent of the magnitude of a pair of CRD images. Thus, the scalar c in Eq (5) can be used to calibrate the approximative CRD to the expected solar CRD. The final calibration for the expected solar CRD is based on the concentrated lunar illuminance measurements and the solar flux density (irradiance) measurements on the target plane.

The verified optical simulations generate all the CRD images in this paper. As Figure 9 shows, the six illuminometers are fixed in the six holes on the white target disk. They are used to figure out the center and the size of the concentration lunar images and reserved for later CRD image calibrations to match the solar CRD. We plan to map the concentrated solar flux distribution of the solar dish using a moving white target with reference heat flux gauges shortly. We can experimentally compare the measured lunar CRD with the solar CRD and verify this new lunar flux mapping model/method.

Figures 1 and 2 illustrate the principle of this new lunar flux mapping model, and the next goal is to transfer it from the simple well-known solar dish concentrator to the complex solar tower concentrator. One potential mothod of reaching this goal is to learn the curve (or function) of "lunar CRD and solar CRD" cosine similarity vs. the corresponding "moon shape and sun shape" cosine similarity and is to find out the number of the smooth-filtering operations for the approximative solar CRD, as Figure 2(a) and (b) show, based on a large number of simulations and measurements on the solar dish concentrator. The learning curves and knowledge are then directly transferred and applied to the solar flux mapping of a solar tower concentrator.

It is reasonable and hopeful that the number of smooth-filtering operations for a well understood solar dish concentrator can be shared for a complex solar tower concentrator. Alternatively, a specially designed reference solar dish concentrator attached with moonlight concentration measuring equipment, like the solar dish test setup in this paper, is synchronously used and combined with the moonlight concentration activities of a solar tower collector for the solar CRD mapping considering the changing environmental conditions. It seems that the latter way is more practical.

Frankly, the new flux mapping method may be less easy in focusing heliostats in a solar power plant because moonlight measurements are performed during the night in a cold environment but will be operating in a warmer daytime environment. This tricky issue may require in-depth mechanical analysis for focusing heliostats.

7. Conclusions

This paper presents a new model to extend the lunar flux mapping of the heliostat field to more moon phases. At this stage, this new lunar flux mapping model is applied to a real solar dish concentrator.

The principle of this lunar flux mapping model recognizes the potential of a solar concentrator to enhance the similarity between the solar CRD and a lunar CRD and that the residual differences between them can be compensated to some extent by using smoothing filtering of the lunar CRD image to obtain the approximative CRD for the expected CRD image.

The new BRT with effective sun/moon shapes for simulation of CRD images of a solar concentrator is developed from the authors' previous BRT with effective sun shape. This general ray-tracing method is applied in all the optical simulations. The compound mirror surface of the solar dish was surveyed using a 3D laser scanner. A uniform triangular mesh for the entire mirror surface was generated to use the BRT with effective moon shapes. The discrete effective sun shape image is the two-dimensional convolution of the discrete Buie sun shape image with the normalized Gaussian error image. It is implemented after inverse FFT (IFFT) of the product of the FFT results of the two images.

The optical simulations and moonlight concentration measurements show good similarities between solar and lunar CRD images, and light source shapes have subtle effects on CRD.

Two typical examples (for the Waning Gibbous moon shape and the Last Quarter moon shape) successfully illustrate how to convert a lunar CRD to the corresponding solar CRD for a dish solar concentrator.

It is hoped that this method can be successfully applied to the complex solar tower concentrator together with the known reference-and-calibration solar dish concentrator.

Acknowledgments

This work was supported by the National Natural Science Foundation of China Project: The mapping method of concentrated solar flux density over the receiver aperture for a solar power tower based on moonlight concentrating tests and real-time measurements of concentrated solar flux from radiometers on the aperture boundaries (No. 61671429). This work was also supported by national research tasks: Working principle and design method of high-temperature particle receiver (2018YFB1501001, affiliated project: Research on key fundamental issues of supercritical CO_2 solar thermal power generation) and study on the structure design and efficient concentration mechanism of planar metasurface solar concentrator (2020YFA0710101, affiliated project: Broad-band planar metasurface solar concentrator and its heat collection system). We like to thank Mr. Mingfei He and Mr. Penglin Huang for their kind helps in the experiments. We are also grateful to Mr. Alex Burton from the Australian Sunopti Company for his control design of the dish concentrator and language editing for this paper.

Conflict of interest

All authors declare no conflict of interest in this paper.

Author contributions

Minghuan Guo: Conceptualization, Methodology, Formal analysis, Investigation, Writing-original draft, Writing-review & editing, Funding acquisition. Hao Wang: Investigation, Data curation. Zhifeng Wang: Supervision, Funding acquisition, Project administration, Writing-Reviewing. Xiliang Zhang: Investigation. Feihu Sun: Investigation. Nan Wang: Investigation.

References

1. Ballestrín J, Burgess G, Cumpston J (2012) Heat flux and temperature measurement technologies for concentrating solar power(CSP), In: Lovegrove, K and Stein, W, *Concentrating solar power technology: Principles, developments and applications,* 1 Eds., Cambridge: Woodhead Publishing Limited, 577–593.
2. Osuna R, Morillo R, Jiménez JM, et al. (2006) Control and operation strategies in PS10 solar plant. *13th SolarPACES Conference*.
3. Ballestrín J (2002) A non-water-cooled heat flux measurement system under concentrated solar radiation conditions. *Sol Energy* 73: 159–168.
4. Ballestrín J, Monterreal R (2004) Hybrid heat flux measurement system for solar central receiver evaluation. *Energy* 2: 915–924.
5. Ballestrín J, Valero J, García G (2010) One-click heat flux measurement device. *16th Solar PACES Conference*.
6. Ballestrín J (2013) Heat flux measurement on CSP. *4th SFERA Summer School*.
7. Kröger-Vodde A, Hollander A (1999) A CCD flux measurement system PROHERMES. *J Phys IV* 9: 649–654.
8. Buck R, Lüpfert E, Tellez F (2000) Receiver for solar hybrid gas turbine and CC systems (REFOS). *Solar Thermal 2000 International Conference*, 95–100.
9. Lüpfert E, Heller P, Ulmer S, et al. (2000) Concentrated solar radiation measurement with video image processing and online flux gauge calibration. *Solar Thermal 2000 International Conference*.
10. Ulmer S, Lüpfert E, Pfänder M, et al. (2004) Calibration corrections of solar tower flux density measurements. *Energy* 29: 925–933.
11. Röger M, Herrmann P, et al. (2011) Flux density measurement on large-scale receivers. *17th SolarPACES Conference*.
12. Ho CK, Khalsa SS, Gill DD, et al. (2011) Evaluation of a new tool for heliostat field flux mapping. *17th SolarPACES Conference*.
13. Ho CK, Khalsa SS (2011) A flux mapping method for central receiver systems. *Proceedings of the 2011 ASME Energy Sustainability Conference*.
14. Ho CK, Khalsa SS (2012) A photographic flux mapping method for concentrating solar collectors and receivers. *J Sol Energy Eng* 134: 041004.
15. Xiao J, Wei S, Wei X, et al. (2015) Solar Flux measurement method for concentrated solar irradiance in solar thermal power tower system (in Chinese). *Acta Opt Sin* 35: 0112003-(1–9).
16. Guo M, Wang Z (2011) On the analysis of an elliptical Gaussian flux image and its equivalent circular Gaussian flux images. *Sol Energy* 85: 1144–1163.
17. Hisada T, Mii H, Noguchi C, et al. (1957) Concentration of the solar radiation in a solar furnace. *Sol Energy* 1: 14–16.
18. Holmes JT (1982) Heliostat operation at the Central-Receiver Test Facility (1978–1980). *Nasa Sti/recon Tech Rep N* 82: 133–138.

19. Hénault F, Royère C (1989) Concentration du rayonnement solaire: analyse et évaluation des réponses impulsionnelles et des défauts de réglage de facettes réfléchissantes. *J Opt (Paris)* 20: 225–240.
20. Siangsukone P, Burgess G, Lovegrove K (2004) Full Moon Flux Mapping the 400 m^2 "Big Dish" at the Australian National University. *Solar 2004: Life, the Universe, and Renewables*, Perth, Western Australia, 3–6.
21. Biryukov S (2004) Determining the optical properties of PETAL, the 400 m^2 parabolic dish at Sede Boqer. *J Sol Energy Eng* 126: 827–832.
22. Lovegrove K, Burgess G, Pye J (2011) A new 500 m^2 paraboloidal dish solar concentrator. *Sol Energy* 85: 620–626.
23. Blázquez R, Carballo J, Cadiz P, et al. (2015). Optical test of the DS1 prototype concentrating surface. *Energy Procedia* 69: 41–49.
24. Salomé A, Chhel F, Flamant G, et al. (2013) Control of the flux distribution on a solar tower receiver using an optimized aiming point strategy: application to THEMIS solar tower. *Sol Energy* 94: 352–366.
25. Wang N, Wang X, Sun F, et al. (2019) Experimental study of moonlight concentration of a solar tower power plant in the full moon night (in Chinese). *Adv New Renewable Energy* 7: 23–31.
26. Guo M, Wang X, Wang N, et al. (2019) Moonlight concentration experiments of Badaling solar tower power plant in Beijing. *AIP Conference Proceedings*, AIPCP20-AR-SolarPACES2019-00046.
27. Wikipedia, Cosine similarity. Wikipedia, 2021. Available from: https://en.wikipedia.org/wiki/Cosine_similarity.
28. Buie D, Monger AG, Dey CJ (2003) Sunshape distributions for terrestrial solar simulations. *Sol Energy* 74: 113–122.
29. Guo M, Sun F, Wang Z (2016) The backward ray tracing with effective solar brightness used to simulate the concentrated flux map of a solar tower concentrator. *22nd Solar PACES Conference*.